White Rose Research Online

eprints@whiterose.ac.uk
https://eprints.whiterose.ac.uk
Universities of Leeds, Sheffield and York

Deposited via The University of Leeds.

White Rose Research Online URL for this paper:
https://eprints.whiterose.ac.uk/id/eprint/241505/

Version: Accepted Version

**Article:**
Shu, W., Chu, D., Cao, Y. et al. (2026) Tropical deforestation, seasonal drought and decline of chemical weathering during the Permian–Triassic transition in southwestern China. Global and Planetary Change, 261. 105437. ISSN: 0921-8181

https://doi.org/10.1016/j.gloplacha.2026.105437

This is an author produced version of an article published in Global and Planetary Change, made available via the University of Leeds Research Outputs Policy under the terms of the Creative Commons Attribution License (CC-BY), which permits unrestricted use, distribution and reproduction in any medium, provided the original work is properly cited.

**Reuse**
This article is distributed under the terms of the Creative Commons Attribution (CC BY) licence. This licence allows you to distribute, remix, tweak, and build upon the work, even commercially, as long as you credit the authors for the original work. More information and the full terms of the licence here: https://creativecommons.org/licenses/

**Takedown**
If you consider content in White Rose Research Online to be in breach of UK law, please notify us by emailing eprints@whiterose.ac.uk including the URL of the record and the reason for the withdrawal request.

UNIVERSITY OF LEEDS
University of Sheffield
UNIVERSITY of York

# Tropical deforestation, seasonal drought and decline of chemical weathering during the Permian–Triassic transition in southwestern China

Wenchao Shu[1, 2], Daoliang Chu[1*], Yiran Cao[1], Haijun Song[1], Paul B. Wignall[3], Jacopo Dal Corso[1], Yuyang Wu[1,4], Li Tian[1], Huyue Song[1], Jinnan Tong[1]

1. State Key Laboratory of Geomicrobiology and Environmental Changes, School of Earth and Planetary Sciences, China University of Geosciences, Wuhan 430074, China

2. School of Earth Resources, China University of Geosciences, Wuhan 430074, China

3. School of Earth and Environment, University of Leeds, Leeds LS2 9JT, UK

4. College of Marine Science and Technology, China University of Geosciences, Wuhan 430074, China

Corresponding author: chudl@cug.edu.cn

**Abstract**

Tropical rainforests are vital biological regulators of global climate, but their vulnerability to catastrophic environmental upheaval is often obscured by the vastness of the geological record. During the end-Permian terrestrial crisis, the demise of the tropical Gigantopteris flora in southwestern China, a key region in the eastern Tethys that preserves exceptional tropical terrestrial records, marked a pivotal breakdown in terrestrial feedbacks, specifically through a substantial decline in chemical weathering. Despite its significance, the temporal coupling and causal relationships between this floral turnover, climatic shifts, and weathering response remain poorly understood. Here, we present a high-resolution reconstruction of sporomorph assemblages, palaeoclimatic indicators, and chemical weathering intensity across the Permian–Triassic transition in southwestern China in the eastern Tethys. Our results document that the region experienced two successive phases of floral crisis. The first phase of crisis involved the collapse of pteridophyte-dominated rainforests, evidenced by a sharp decline in wetland taxa. This was followed by a second phase of crisis marked by the demise of previously thriving isoetalean herbaceous communities. These floral changes were closely linked to a progressive shift in climate, characterized by intensifying seasonal drought, as indicated by increased wildfire activity and the expansion of xerophytic vegetation. Notably, chemical weathering did not decline synchronously with the first phase of initial rainforest loss but remained elevated until the subsequent loss of isoetaleans under enhanced aridity, after which it underwent a

marked and prolonged reduction that persisted throughout the Early Triassic. The two-phase floral crisis, climatic fluctuations, and the decline in chemical weathering underscore the intricate feedback loops between vegetation, climate, and weathering, highlighting the need to refine mechanistic representations of these processes in Earth system models.

**Keywords:** Permian–Triassic transition, tropical deforestation, drought, chemical weathering, southwestern China

## 1. Introduction

Plant abundance and diversity are key components of a functioning ecosystem, both in geological history and modern times (Tilman et al. 2014; Hull and Darroch 2017; Dunhill et al. 2024). However, deforestation poses significant threats to these ecosystems, causing habitat destruction, carbon release, desertification, soil erosion, and flooding, which collectively endanger biodiversity, climate stability, and water availability (Chakravarty et al., 2012). Additionally, deforestation reduces chemical weathering, a critical process for atmospheric $CO_2$ consumption, thereby weakening the climate feedback mechanism (Berner, 1992). Understanding these dynamics is crucial for addressing modern deforestation and biodiversity loss.

The Permian–Triassic mass extinction (PTME), the most severe bio-crisis of the Phanerozoic, resulted in the loss of approximately 81% of marine species and 70% of terrestrial vertebrate families (Benton, 2016; Stanley, 2016; Fan et al., 2020). It coincided with a widespread collapse of terrestrial flora across diverse geographic and

57 climatic zones, and lead to the Early Triassic "coal gap" (e.g., Retallack et al., 1996;
58 Xu et al., 2022). Although regional variations in plant responses to extinction have
59 been noted (Fielding et al., 2019; Feng et al., 2020a; Chu et al., 2025), and some
60 studies suggest that plant extinctions were less severe than those of animals
61 (Schneebeli–Hermann et al., 2017; Nowak et al., 2019), the PTME is widely regarded
62 as the most catastrophic event for terrestrial flora (McElwain and Punyasena, 2007;
63 Cascales–Miñana et al., 2016). The collapse of terrestrial ecosystems during the
64 Permian–Triassic mass extinction (PTME) is widely attributed to extreme global
65 warming and a cascade of associated environmental crises—including widespread
66 wildfires, acid rain, accelerated soil erosion, and stratospheric ozone depletion. These
67 disturbances were primarily driven by massive volcanic emissions of $CO_2$, $SO_2$, and
68 halogens, further amplified by intensified El Niño–Southern Oscillation (ENSO)
69 activity (Sephton et al., 2015; Benton et al., 2018; Wu et al., 2021; Dal Corso et al.,
70 2024; Sun et al., 2024; Chu et al., 2025). Although elevated temperatures would
71 theoretically enhance chemical weathering, concurrent aridification and vegetation
72 degradation likely suppressed weathering fluxes, thereby destabilizing the Earth's
73 natural weathering–climate negative feedback system (Yang et al., 2022; Xu et al.,
74 2023). While the relationships among floral changes, climate perturbations, and
75 chemical weathering processes have been well-documented in middle-high latitudes
76 such as eastern Australia (Fielding et al., 2019; Vajda et al., 2020; McLoughlin et al.
77 2021), comparable high-resolution, integrated records have been lacking for South
78 China. Consequently, the precise temporal sequencing and causal linkages among

rainforest ecosystem collapse, climatic shifts, and weathering responses in equator region remain unresolved (Chen et al., 2022, 2025; Yang et al., 2022; Xu et al., 2023). The hypothesized synchronicity of these processes thus remains speculative, awaiting rigorous validation through high-resolution geological archives.

To address this gap, we analyzed sporomorphs to reconstruct the high-resolution floral dynamics and assess paleoclimatic conditions in the Permian–Triassic interval in South China. In addition, we assessed the chemical index of alteration (CIA; Nesbitt and Young, 1982) and mafic index of alteration (MIA; Babechuk et al., 2014) to evaluate changes in weathering intensity. Our findings provide new constraints on the sequence of events during Earth's most severe mass extinction, with important implications for understanding vegetation-climate-weathering feedback under extreme warming scenarios.

## 2. Geological settings

South China was located near the palaeoequator (about 0°–10°N) during the Permian–Triassic (P–Tr) transition (Fig. 1A, Scotese 2021). We examined the continental P–Tr transition in the cored borehole ZK4703, drilled 15 km south of Fuyuan County, southwestern China (GPS: 25.54151°N, 104.28994°E; Fig. 1B). The transitional sequence can be divided into the Xuanwei and Kayitou formations in ascending order in ZK4703. The Late Permian Xuanwei Formation is dominated by greyish yellow and green sandstones, greyish yellow mudstones and silt-mudstones, grey siltstones and coal beds. This stratigraphic unit has been interpreted as floodplain,

peat deposits, and channel sandstone bodies (Bercovici et al., 2015; Wignall et al., 2020) and has yielded a high-diversity plant assemblage of the *Gigantopteris* flora (Yu et al., 2015; Feng et al., 2020a). The latest Permian into earliest Triassic Kayitou Formation is composed of massive greyish green silt-mudstones with few interbedded calcareous sandstones, but lacks coal, and is considered to record low-energy paralic conditions (Fig. 2, Bercovici et al., 2015; Wignall et al., 2020). A low diversity floral assemblage is dominated by Peltaspermales and *Tomiostrobus* in the Kayitou Formation (Yu et al., 2010; Feng et al., 2020a).

## 3. Materials and methods

We sampled a 30-meter interval at an average spacing of 0.9 m, with higher resolution sampling (0.47 m spacing) across the critical 7-meter transition from the uppermost Xuanwei Formation to the lowermost Kayitou Formation (Fig. 2). For palynological analysis, thirty-one productive palynological mudstone samples from ZK4703 were processed. These fresh mudstone samples were crushed, weighed (20–30 g for each sample) and then processed by hydrochloric acid (HCl) and hydrofluoric acid (HF) for maceration. The residues were subject to zinc chloride heavy liquid separation (2.2 g/cm$^3$) and sieved through a 7 μm mesh. The resultant organic residues were mounted on permanent microscope slides using neutral balsam. Sporomorphs on the slides were counted on a Zeiss Axio Scope A1 microscope, until ≥100 specimens were counted, or ten entire slides were scanned (more than 300 grains for each sample in 19 samples; more than 200 grains in seven samples and more than 100 in five

121 samples) (Table S1). Palynological assemblages were defined by cluster analysis with
122 Euclidean distance metric in PAST software (Hammer et al., 2001). And the
123 palynological diagram was performed in C2 software (Juggins, 2007). We adopted the
124 classification of wetland and dryland sporomorphs (DiMichele et al., 2006; DiMichele,
125 2014). Proportional sporomorph abundance in assemblages is quantified as abundant
126 (>50%), common (10–50%), frequent (1–10%) and rare (<1%) after Smith and
127 Butterworth (1967). For semi-quantitative evaluation of humid/dry climate variations,
128 we employed the xerophytic/hygrophytic (X/H) ratio by categorizing the 40 identified
129 genera into 8 moisture-related sporomorph groups, including both hygrophytes and
130 xerophytes (Visscher and van der Zwan 1981; Galfetti et al. 2007). All the raw
131 palynological data is in the Supplemental Material.
132 Zsx Primus II wavelength dispersive X-ray fluorescence spectrometer (XRF)
133 was used for the analysis of major elements in the whole rock. Results were calibrated
134 using both GSS07401-08 and internal laboratory standards. Analytical precision based
135 on replicate analyses was better than ± 2% for all major elements. Trace element
136 analysis of whole rock was conducted on Agilent 7700e ICP-MS with an analytical
137 accuracy of <10%. Additionally, organic carbon isotopes ($\delta^{13}C_{org}$), total of organic
138 carbon (TOC), Hg and Hg/TOC data of the ZK4703 are available from our previous
139 work (Chu et al., 2020).
140 Chemical Index of Alteration (Nesbitt and Young, 1982) is widely used as a
141 measure of chemical weathering and is calculated as: $CIA = Al_2O_3 / (Al_2O_3 + CaO^* + Na_2O + K_2O) \times 100$ (1). All the major element oxides are given in molar proportion
142

and CaO* represents molar proportion of CaO specific in silicates. CaO* = min [(CaO - 10/3 × $P_2O_5$), ($Na_2O$)] (McLennan, 1993). To exclude the influence of diagenesis, pre-alteration molar $K_2O$ was calculated using the method introduced by Panahi et al. (2000): $K_2O_{corr.} = [m \times Al_2O_3 + m \times (CaO^* + Na_2O)] / (1 - m)$, and $m = K_2O / (Al_2O_3 + CaO^* + Na_2O + K_2O)$ (2) is calculated for the parent material (which in our case is mainly the regional Emeishan Basalt). The A-CN-K diagram shows that the vast majority of the samples were not significantly affected by the K-metasomatism except zk-61 (Fig. S1; Table S5). The corrected CIA, noted as $CIA_{corr.}$ is $[Al_2O_3 / (Al_2O_3 + Na_2O + K_2O_{corr.} + CaO^*)] \times 100$ (3). The Mafic Index of Alteration (MIA), often used to indicate the weathering intensity of a ferrimafic basal (Babechuk et al., 2014), is calculated as: $[(Al_2O_3 + TFe_2O_3)/ (Al_2O_3 + TFe_2O_3 + MgO + Na_2O + K_2O + CaO^*)] \times 100$ (4). Here CIA, CIAcorr. and MIA were calculated across the Permian–Triassic boundary (PTB) in ZK4703 (Table S5). All the raw chemical weathering data is in the Supplemental Material.

## 4. Results

### 4.1. Palynology

The palynological analysis of core ZK4703 reveals five distinct floral assemblages during the Permian–Triassic transition based on the relative abundance of spore and pollen taxa stratigraphically upwards (Fig. 2). The *Leiotriletes–Yunnanospora–Tripartites* assemblage (Assemblage 1) is recorded from the depths of 674.50 m to 690.00 m interval in the upper part of the Xuanwei formation and the base of the

Kayitou formation (Fig. 2). It was marked by the common *Leiotriletes* spp. (12.4%–38.2%), frequent *Yunnanospora* spp. (2.7%–6.9%) and *Tripartites* spp. (0.4%–3.4%).

The *Crassispora–Eupunctisporites* assemblage (Assemblage 2) was recovered from the 672.00 m to 674.50 m interval of the lower part of Kayitou Formation (Fig. 2). It is named by the appearance of *Eupunctisporites* spp. (1.6%–5.2%), increased *Crassispora* spp. (0.6%–4.0%). It also contains common *Aratrisporites* spp. (20.0%–34.1%, 26.6% on average), frequent-common *Alisporites* spp. (0.6%–20.1%), common *Leiotriletes* spp. (13.1%–21%). The spore tetrads were rare to frequent (0.6%–1.3% in total sporomorphs and 0.6%–1.6% in total spore grains). Charcoal abundance shows a clear peak value of 1394–2034 particles per 100 grams of bulk rock in the strata in which the *Crassispora–Eupunctisporites* assemblage occurs, representing a significant increase compared to the background level of 10–280 particles per 100 grams observed in the first assemblage (Chu et al., 2020, Fig. 7).

The *Aratrisporites* assemblage (Assemblage 3, 670.45 m~672.00 m interval, Fig. 2) is marked by abundant *Aratrisporites* spp. (63.6%), common *Leiotriletes* spp. (5.8%–13.3%), frequent *Laevigatosporites* spp. (0.9%–11.0%) and frequent *Alisporites* spp. (0.6%–8.7%). There is also a remarkable spore tetrad spike in this assemblage (Table S3 and Chu et al. 2021; 15.6%–18.6% in total sporomorphs and up to 15.8%–19.4% in total spore grains).

The *Alisporites–Vesicaspora–Laevigatosporites* assemblage (Assemblage 4, 669.00 m~670.45 m interval, Fig. 2) were marked by abruptly increased *Alisporites* spp. (10.0%~12.0%, average 16.0%), *Vesicaspora* spp. (1.0%~24.0%, average 12.1%)

and *Laevigatosporites* spp. (8.2%~18.0%, average 11.1%).

The *Alisporites–Platysaccus* assemblage (Assemblage 5, 661.75 m~669.00 m interval, Fig. 2), marked by abundant *Alisporites* spp. (19.0%–46.7%) and common *Platysaccus* spp. (9.0%–33.0%) and frequent *Chordasporites* spp. (2.0% on average). Trilete or monolete spores are less frequent (1.2% on average).

### 4.2. Xerophytic/Hygrophytic ratios

All spores and pollens were assigned to two categories based on water ecological adaptability of the parent plants, including hygrophytic and xerophytic elements (Table S2). The ratio between hygrophytes and xerophytes (X/H ratio) of ZK4703 goes through three-phases evolution in ascending order (Fig. 3). In the first phase (phase I: 674.50 m–690.00 m interval), very low X/H ratios show the dominant hygrophytes (96.5% on average) include abundant trilete azonate spores (53.4% on average), common monolete azonate spores (average 15.2%), common alete spores (average 23.2%) and frequent *Aratrisporites* group (average 1.8%).

The second phase (phase II: 669.00 m–674.50 m, Fig. 3) shows low but fluctuant X/H ratios (1.7%–52.6% , 23.8% on average). It is dominated by hygrophytic sporomorphs but there are also some xerophytes present (Fig. 3). The hygrophytes mainly consist of abundant herbaceous isoetaleans (especialy of *Aratrisporites* group, Fig. 4), common pteridophyte trilete/monolete azonate spores. Xerophytes mainly consist of gymnosperm non-striate pollen grains.

The third phase (phase III: 661.75 m–669.00 m, Fig. 3) is characterised by

highest X/H ratio (56.0%–74.8%, 66.1% on average ) with an even greater abundance of xerophytes (average 63.6%, 52.8%~72.2%, Fig. 3). The conifer/pteridosperm non-striate bisaccate pollens are abundant and taeniate/striate bisaccate pollens also get an increase, while the hygrophytes (e.g. pteridophyte trilete or monolete spores and herbaceous isoetaleans of *Aratrisporites* spp.) became less frequent or rare in the third phase.

### 4.3 Chemical weathering data

CIA values remain consistently high (~92) in the Xuanwei Formation and the base of the Kayitou Formation (Table S5). Subsequently, there is an abrupt drop of CIA from 90 to 75 in the lower Kayitou Formation, approximately 6 m above both the onset of the negative carbon isotope excursion (CIE) at a level around the transition from assemblages 4 and 5 that record the rise to dominance of xerophytic gymnosperm flora. The $CIA_{corr.}$ shows a similar range and stratigraphic variation to the CIA (Table S5). The MIA values display comparable trends, varying between 65 and 85. Like the CIA, MIA maintains elevated values (80–85) from the Xuanwei Formation into the basal Kayitou Formation, and then abruptly decreases like the CIA pattern (Table S5).

## 5. Discussion

### 5.1. Two-phase tropical floral crisis during the Permian–Triassic transition

During the latest Permian, the flora of southwestern China was characterized by

227 a pteridophyte-dominated rainforest ecosystem, as evidenced by both megafossil
228 plants of the *Gigantopteris* flora (Yu et al., 2015; Zhang et al., 2016; Chu et al., 2016;
229 Feng et al., 2020a; Xu et al., 2022) and the *Leiotriletes–Yunnanospora–Tripartites*
230 palynological assemblage identified in our study section (Fig. 4). This assemblage is
231 consistent with other late Changhsingian palynofloras from South China, including
232 the *Yunnanospora radiata–Gardenasporites* spp. assemblage (Ouyang, 1986), the fern
233 spore-dominated assemblage associated with the *Gigantopteris* megaflora (Yu et al.,
234 2008), and the *Crassispora orientalis–Anticapipollis tornatilis* assemblage (Shao et
235 al., 2023). In contrast, contemporaneous Southern Hemisphere assemblages were
236 dominated by glossopterid taeniate bisaccate pollen and other gymnospermous non-
237 taeniate pollen types (Fig. 5, Lindström and McLoughlin, 2007; Schneebeli-Hermann
238 et al., 2015; Liu et al., 2020; Vajda et al., 2020, 2023), while the Northern Hemisphere
239 featured abundant pteridosperm and conifer pollen, including *Lueckisporites* spp.,
240 other taeniate bisaccates, the *Vittatina* group, and various non-taeniate forms (Fig. 5,
241 Hou, 2004; Cao et al., 2008; Chu et al., 2016, 2025; Hochuli et al., 2010b; Diez et al.,
242 2014; Schneebeli-Hermann et al., 2017; Jewuła et al., 2021; Shu et al., 2023; Peng et
243 al., 2025). These patterns reflect a clear latitudinal gradient during the latest Permian,
244 tropical regions supported pteridophyte-dominated rainforest palynofloras, while
245 temperate to cool climatic zones were characterized by gymnosperm-dominated
246 assemblages.

247 Subsequently, the Permian–Triassic tropical flora underwent an extreme
248 ecological crisis (the crisis interval encompassing Assemblages 2–4), manifested as

two successive, distinct phases of vegetation turnover (Fig. 4). The first phase is marked by a significant decline in megafossil plant diversity near the last coal bed in southwestern China (Yu et al., 2015; Bercovici et al., 2015; Chu et al., 2020; Feng et al., 2020a). Palynological data from our study reveal that this crisis was characterized by a pronounced decrease in wetland taxa abundance, signaling the collapse of the pteridophyte-dominated rainforest (Fig. 4). Then, abundant fungal cysts fossils, pronounced charcoal peaks, the onset of a negative $\delta^{13}C_{org}$ excursion, and a marked reduction in TOC are recorded (Fig. 5; Yu et al., 2008; Bercovici et al., 2015; Chu et al., 2020). These features closely parallel the "dead zone" documented in eastern Australia, which is characterized by the collapse of *Glossopteris*-dominated wetland floras, elevated charcoal abundances, the onset of a negative excursion, and reduced TOC values (Vajda et al., 2020; Mays et al., 2021; McLoughlin et al., 2021). Following this potential "dead zone" phase, isoetalean lycophytes (e.g., *Aratrisporites*, *Lundbladispora*, and *Kraeuselisporites*) proliferated, with *Aratrisporites* attaining a pronounced peak in Assemblage 3 (Fig. 2). This palynological signal is consistent with the stratigraphic radiation of the *Tomiostrobus–Lepacyclotes* megafossil flora (Yu et al., 2015; Feng et al., 2020a; Xu et al., 2022) and reflects opportunistic colonization by herbaceous isoetalean lycopsids in the aftermath of rainforest collapse (Feng et al., 2020a; Xu et al., 2022). Comparable peaks in isoetalean lycophyte spores have been widely documented in the earliest Triassic across both hemispheres and a broad range of paleolatitudes (Hochuli et al., 2010b; Schneebeli-Hermann et al., 2015, 2017; Liu et al., 2020; Vajda et al., 2023). Additionally, exceptionally abundant spore

271 tetrads occur in southwestern China during this interval (Fig. 4; Table S3), closely
272 mirroring coeval records from both the Northern Hemisphere (middle–high latitudes:
273 Russia, Xinjiang, East Greenland, Arctic Canada, Norway; low latitudes: Italy,
274 Hungary, Meishan) and the Southern Hemisphere (middle–high latitudes: Kenya
275 [Mombassa Basin], Argentina, Madagascar, Western Australia; low latitudes: India,
276 Sri Lanka) (Balme, 1963; Hankel, 1992; Looy et al., 2005; Hochuli et al., 2010a, b;
277 Gutiérrez et al., 2017). These tetrads are commonly attributed to stress-tolerant,
278 opportunistic isoëtalean lycopsids adapted to wet habitats (Looy et al., 2005, 2021).
279 Notably, peak tetrad abundances closely coincide with elevated Hg and Cu
280 concentrations, pointing to widespread heavy-metal toxicity associated with
281 volcanism (Chu et al., 2021), potentially exacerbated by enhanced UV-B radiation
282 (Visscher et al., 2004).

283 Concurrently, drought-adapted conifers and pteridosperms (e.g., *Alisporites* spp.,
284 *Vesicaspora* spp., *Platysaccus* spp., *Lunatisporites* spp., *Protohaploxypinus* spp.)
285 began to diversify, albeit remaining relatively scarce (Figs. 2, 4). These changes
286 collectively signify the collapse of the formerly stable pteridophyte-dominated
287 rainforest under increasingly seasonal and arid climatic conditions. Although global
288 sporomorph data indicate only a moderate genus-level extinction rate (17%; Nowak et
289 al., 2019), this interval was marked by multiple interrelated ecological disturbances.
290 These include spikes in algal, fungal, and lycophyte spores; widespread sporomorph
291 rarity accompanied by reduced total organic carbon (TOC); the onset of a carbon
292 isotope excursion (CIE); intensified wildfire activity (evidenced by abundant charcoal,

293 Fig. 4); enhanced soil erosion; heavy metal toxicity (e.g., elevated Hg loading, Fig. 6);
294 and persistent seasonal aridity. This combination of stressors defines the interval as a
295 "dead zone" (Fig. 5, Hochuli et al., 2010b; Visscher et al., 2011; Vajda et al., 2020;
296 Mays et al., 2021; Chu et al., 2020, 2021; Wu et al., 2023), reflecting a fundamental
297 ecosystem reorganization in which stress-tolerant taxa replaced rainforest vegetation
298 under intensely stressful conditions.
299 The second phase of the crisis, unfolding in the earliest Triassic, saw a
300 pronounced decline in South China of the isoetalean taxa that had previously
301 expanded following the first phase of the crisis (Schneebeli-Hermann, 2020; Looy et
302 al., 2021; Figs. 6, 7). This decline represents the loss of the moisture-sensitive
303 isoetalean herbland communities that had previously expanded. In their place,
304 drought- and heat-tolerant shrub communities dominated by pteridosperms and
305 conifers became fully established (Figs. 2, 4). This new assemblage included
306 abundant pteridosperms (e.g., *Alisporites* spp., likely Peltaspermales), common
307 conifers (e.g., *Platysaccus* spp., *Vesicaspora* spp., *Chordasporites* spp.), and other
308 frequent pteridosperms (e.g., *Lunatisporites* spp., *Protohaploxypinus* spp.,
309 *Striatopodocarpites* spp.). This pronounced increase in gymnospermous pollen is well
310 documented in terrestrial facies of South China (Fig. 5, Ouyang, 1986; Zhang et al.,
311 2016; Xu et al., 2022; Shao et al., 2023) and even in the marine GSSP section at
312 Meishan (Fig. 5, Ouyang and Utting, 1990; Zhang et al., 2007; Schneebeli-Hermann
313 and Galasso, 2025). It reflects not only rapid colonization by Peltaspermalean-
314 dominated shrub communities in the post-crisis interval (Figs. 2, 4) but also an

adaptive response to increasingly arid and high-temperature conditions (Lancaster and Humphreys, 2020; Xu et al., 2025). Both Induan and Olenekian megafloras in South China exhibit gymnosperm-dominated assemblages rather than isoetalean dominance (Feng et al., 2018; Broutin et al. 2020; Schneebeli-Hermann and Galasso, 2025). Thus, the second phase of tropical floral crisis significantly impacted the wetland taxa—particularly isoetalean lycopsids—leading to their reduced representation in the latter periods of the Early Triassic in tropical regions, a change that may have forced their migration to higher latitudes.

### 5.2. Climatic aridification triggers vegetation collapse and weathering decline

Our results reveal a distinct climatic transition during the crisis interval in southwestern China (Fig. 6). Although maintaining an overall low average X/H ratio (0.238), the marked fluctuations (0.017–0.526) coupled with frequent wildfire evidence clearly indicate increasing climatic instability and seasonal drought stress (Fig. 6; Sun et al., 2024; Chu et al., 2025). Besides, there is one pronounced humid pulse (X/H ratio: 0.017–0.166, average 0.079), which is correlated to the assemblage 3. This humid pulse foster the flourishing of herbaceous isoetalean lycophytes (Fig. 6) after the collapse of rainforests. The post-crisis period saw the aridity trend accelerate dramatically, with X/H ratios surging to 0.560–0.748 (average 0.661), reflecting substantially enhanced dry intervals under continued global warming. This caused the demise of moisture-dependent wetland flora while simultaneously promoting the expansion of drought-adapted dryland gymnosperm shrub communities (Fig. 7).

Crucially, multiple lines of evidence, including the wildfire record, palynological turnover, and X/H ratios, collectively demonstrate rainforest collapse in South China coincides with intensifying seasonal drought, a likely cause-and-effect scenario. There are parallels with modern Amazonian rainforest ecosystems, where intensifying seasonal drought and associated wildfires are causing rainforest degradation (Flores et al., 2024). This climate-driven vegetation transformation subsequently exerted a profound influence on terrestrial weathering processes (Fig. 7). The intensity of chemical weathering is affected by temperature, precipitation, physical erosion, lithology of parent rocks and vegetation coverage (Kump et al. 2000; Brantley et al., 2023). Previous studies show that forest dieback and associated soil erosion enhanced physical weathering while reducing water availability and shifting to kinetic-limited weathering regimes. This likely counteracted the effect of temperature-enhanced weathering kinetics and thus caused the decline of chemical weathering seen during the PTME (Chen et al. 2022; Yang et al. 2022; Xu et al. 2023). However, it has hitherto been unclear if there is a synchronicity between the floral extinctions and suppressed chemical weathering in South China.

Source rock composition plays a vital role in controlling the mineralogy and geochemistry of sediments, while physical sedimentation processes, through hydraulic sorting or recycling of specific grains and minerals, may further modify chemical weathering proxy values by constraining sediment composition (Garzanti et al., 2010, 2011; Garzanti and Resentini, 2016). To evaluate the potential influences of provenance variability and sediment recycling on our geochemical records, we

conducted trace element analyses. The relatively invariant $TiO_2/Al_2O_3$, Zr/Ti, Th/Sc, Zr/Sc, and Cr/Th ratios throughout the studied succession, together with consistently low Th/Sc and Cr/Th values, indicate negligible sorting and recycling during deposition and a stable provenance with minimal recycled crustal input (Table S6). These results confirm that primary geochemical signals have not been significantly overprinted by sedimentary processes. Additionally, index of compositional variability (ICV) values ranging from 0.87 to 1.85 (mean = 1.31) suggest that the studied samples are derived from immature sediments with no significant recycling (Cox et al., 1995).

The extreme chemical weathering intensity in Late Permian southwestern China, as indicated by elevated CIA and MIA values (Fig. 7, 8), which were notably greater than values elsewhere (Xu et al., 2023) was likely due to the warm-humid tropical conditions, presence of readily weathered basalts (the Emeishan flood basalts), and dense pteridophyte rainforests. These rainforests are postulated to have contributed to intense weathering through organic acid production and canopy water retention (Fig. 7; Yang et al. 2022; Xu et al. 2023). However, contrary to this scenario, our data reveal that strong chemical weathering persisted with disturbances after the collapse of rainforests and establishment of herbaceous vegetation (Fig. 7, 8). This is likely because persistently seasonal climates with prolonged wet conditions maintained essential moisture availability (Chu et al., 2025), while opportunistic herbaceous communities, recently shown to possess high chemical weathering efficiency (Larsen et al., 2023), actively contributed to weathering processes. In addition, DBF/TOC data

(detrital biomarker fossil) reveals a pulse of intensified soil erosion following deforestation (Wu et al., 2023), which further promoted weathering by exposing fresh rock surfaces. Moreover, a brief episode of extreme humidity not only promoted the proliferation of herbaceous isoetalean lycophytes but was also associated with a slight decline in chemical weathering intensity (as indicated by slightly lower CIA values) and the most intense soil erosion, as reflected by the highest DBF/TOC ratios. Subsequently, intensifying aridity caused the disappearance of herbaceous isoetalean vegetation, reduced plant cover, and shorter water/rock contact due to seasonal drought-extreme precipitation cycles, collectively diminishing water availability for silicate weathering. Ultimately, the shift from supply-limited to kinetic-limited weathering regimes, with physical weathering surpassing chemical processes, led to prolonged weathering reduction into the Early Triassic (Yang et al. 2022; Chen et al. 2022, 2025; Xu et al. 2023).

Our results demonstrate that the Permian–Triassic disturbances in chemical weathering in southwestern China were closely linked to the collapse of rainforest ecosystems. However, the pronounced decline in chemical weathering occurred after the crisis interval and was more strongly associated with the loss of wetland flora. The disturbances in chemical weathering during the crisis interval were mitigated by the proliferation of herbaceous colonizers and relatively high moisture levels, within the context of a highly seasonal climate (Fig. 8). This indicates a delay in the breakdown of the weathering-climate regulatory system, highlighting a previously unrecognized resilience in terrestrial ecosystems. In some regions, post-extinction lycopsid-

dominated vegetation and increased intervals of precipitation in an overall arid climate may explain observations of slightly enhanced weathering (Cao et al., 2019; Frank et al., 2021; Xu et al., 2023). However, escalating temperatures ultimately amplified seasonal aridity and extreme rainfall (Sun et al. 2024), reducing vegetation density and accelerating physical weathering, and were the ultimate drivers of chemical weathering decline in the Early Triassic.

## 6. Conclusions

The Permian–Triassic tropical flora crises in southwestern China unfolded in two distinct phases, the collapse of the pteridophyte-dominated rainforest ecosystem followed by the demise of isoetalean-dominated herblands. These sequential wetland vegetation shifts were driven by progressively intensifying seasonal aridification, which not only directly triggered floral turnover but also fundamentally suppressed chemical weathering regimes. The decline in weathering efficiency, in turn, impaired the Earth's climate regulation capacity, establishing a critical positive feedback loop. This self-reinforcing cascade, where aridification drove deforestation, which then reduced weathering, further exacerbating climatic extremes, ultimately pushed the terrestrial ecosystem beyond a tipping point. The breakdown of the vegetation-climate-weathering system led to the irreversible loss of the Late Permian rainforest biome, with its consequences enduring throughout the Early Triassic. Our study underscores the indispensable role of vegetation in maintaining Earth surface stability and reveals the particular vulnerability of tropical ecosystems to coupled climatic and

weathering feedbacks under high-stress conditions. This deep-time analogue provides a mechanistic framework for understanding terrestrial ecosystem resilience—or lack thereof—in the face of rapid environmental change.


## Acknowledgments

This study was supported by the National Key Research and Development Project of China (Grant No. 2024YFF0808100), the National Natural Science Foundation of China (grants 42030513, 42472021, 42172031) and the China Postdoctoral Science Foundation (2023M733298). We also thank Yao Wang for assistance in field sampling and palynological preparation. We are grateful to Christopher R. Fielding and Elke Schneebeli for their time and meticulous evaluations. Their rigorous and thoughtful reviews significantly strengthened the clarity and scientific impact of this study.


## Figure captions

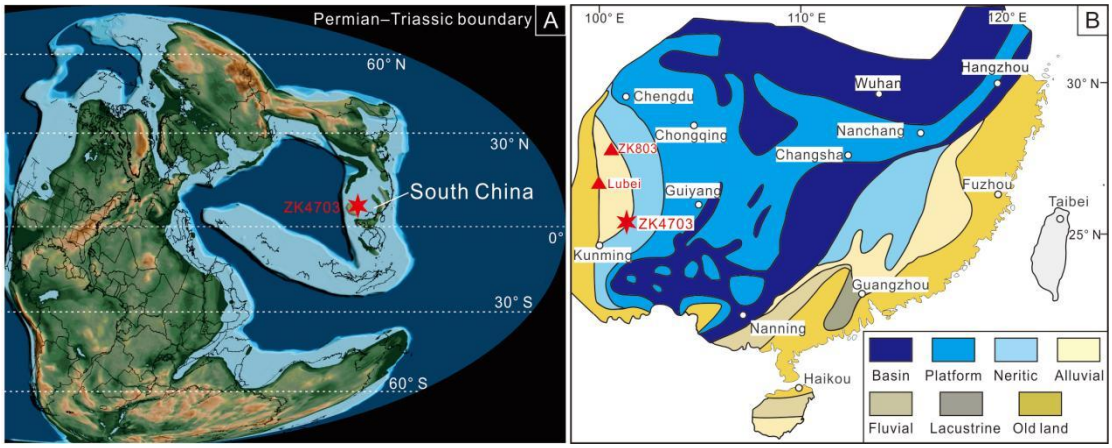


**Figure 1.** Palaeogeographical setting of study area during Permian–Triassic transition. A. Global palaeogeographical map and the locality of study area; B. South China palaeogeography and location of study section (ZK4703) and other previous study

sections (Lubei and ZK803 sections from Xu et al. 2017; Zhang et al. 2016, 2021).

Base map is after Scotese (2021) and Zheng (2011).

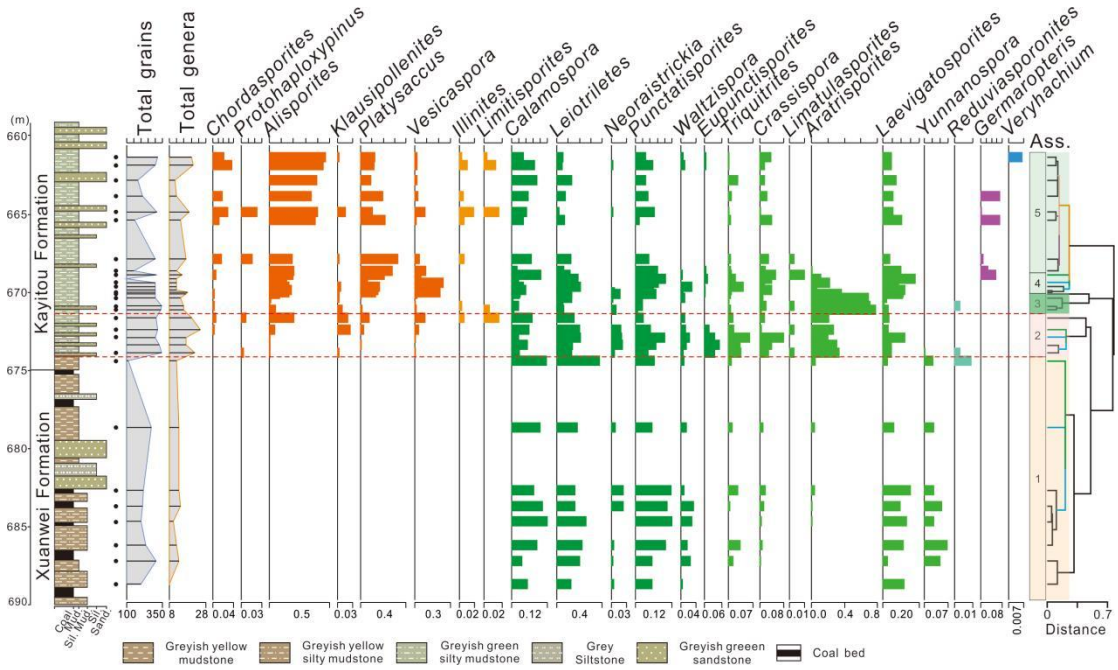


**Figure 2.** The lithological column and the distribution of different most common genera of sporomorphs. Ass., palynological assemblages. Palynological assemblages defined by cluster analysis with Euclidean distance metric in PAST software. Assemblages 1–5: the *Leiotriletes–Yunnanospora–Tripartites* assemblage (Assemblage 1); *Crassispora–Eupunctisporites* assemblage (Assemblage 2); *Aratrisporites* assemblage (Assemblage 3), *Alisporites–Vesicaspora–Laevigatosporites* assemblage (Assemblage 4) and *Alisporites–Platysaccus* assemblage (Assemblage 5).

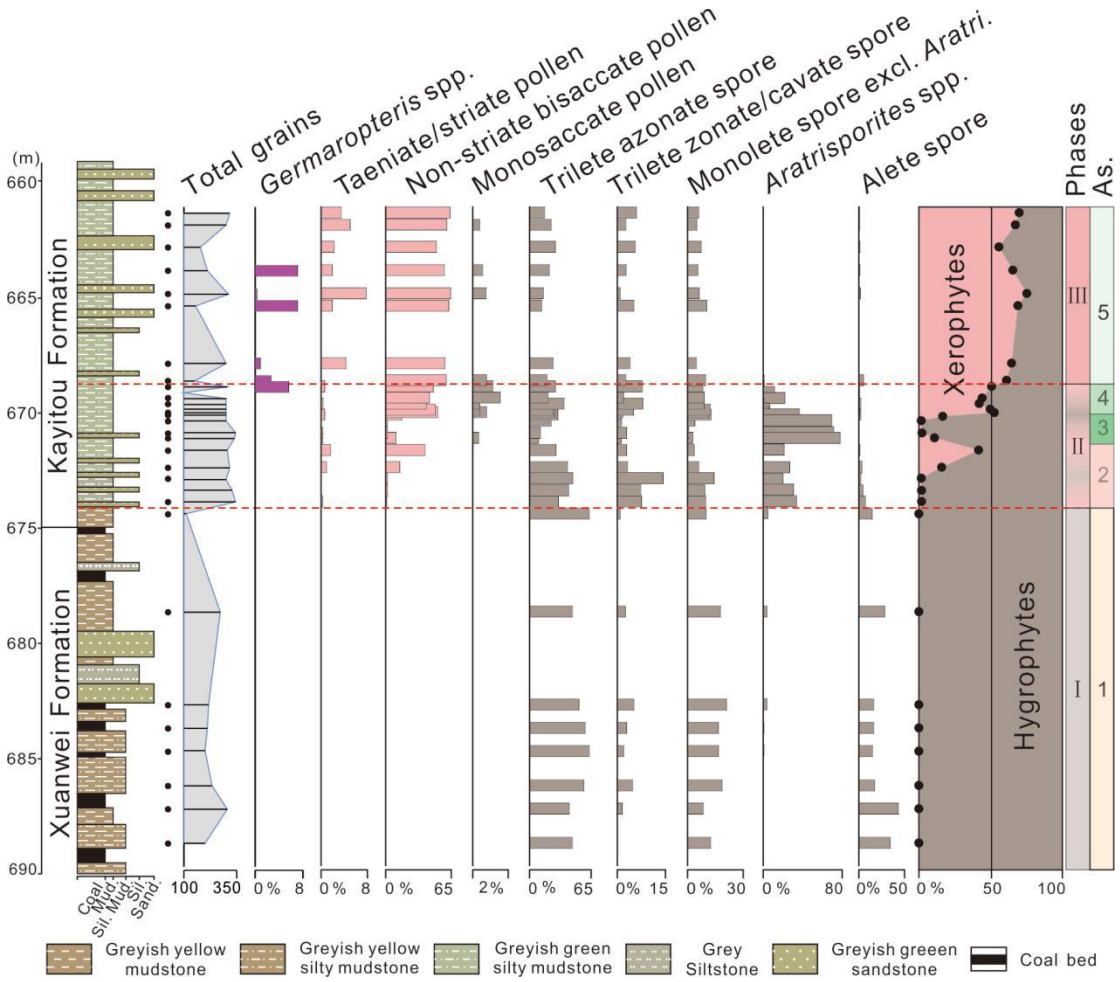


449 **Figure 3.** Abundance of the xerophyte and hygrophyte groups, cuticle of

450 *Germaropteris* spp. and X/H ratios across the Permian–Triassic boundary at ZK4703,

451 excl., excluding; *Aratri*., *Aratrisporites* spp.

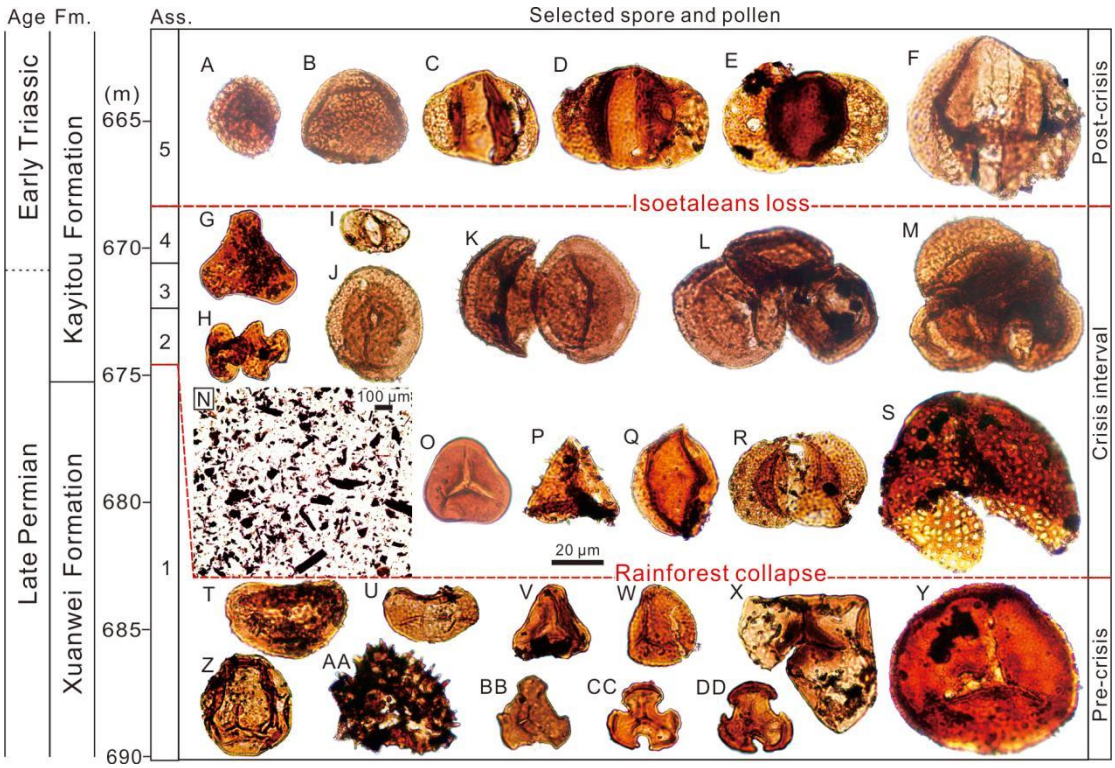


452 **Figure 4.** Fossil sporomorphs before, during and after the crisis interval. A,

453 *Lundbladispora* sp., slider No.: ZK4703_ZK52; B, *Verrucosisporites* sp., slider No.:

454 ZK4703_ZK52; C, D, *Alisporites* spp., slider No. of C: ZK4703_ZK39, slider No. of

455 D: ZK4703_ZK45; E, *Platysaccus* sp., slider No.: ZK4703_ZK51; F,

456 *Protohaploxypinus* sp., slider No.: ZK4703_ZK52; G, *Waltzispora strictura*, slider

457 No.: ZK4703_ZK33.5; H, the spore dyad or broken spore tetrad of *Waltzispora*

458 *yunnanensis*, slider No.: ZK4703_ZK33.5; I, *Vitreisporites* sp., slider No.:

459 ZK4703_ZK34; J, *Aratrisporites* sp., slider No.: ZK4703_ZK33; K, the broken spore

460 tetrad of *Aratrisporites parvispinosus*, slider No.: ZK4703_ZK33; L, the broken spore

461 tetrad of *Aratrisporites* sp., slider No.: ZK4703_ZK33; M, one spore tetrad of

462 *Aratrisporites* sp., slider No.: ZK4703_ZK33; N, predominance of black opaque

463 woody phytoclasts and few bisaccate pollens, slider No.: ZK4703_ZK32; O,

*Leiotriletes directus*, slider No.: ZK4703_ZK31; P, *Neoraistrickia* cf. *loganensis*, slider No.: ZK4703_ZK29; Q, *Aratrisporites yunnanensis*, slider No.: ZK4703_ZK23; R, *Vesicaspora* sp., slider No.: ZK4703_ZK29; S, *Eupunctisporites chinensis*, slider No.: ZK4703_ZK25; T, *Yunnanospora radiata*, slider No.: ZK4703_ZK16; U, *Laevigatosporites minor*, slider No.: ZK4703_ZK16; V, *Leiotriletes exiguus*, slider No.: ZK4703_ZK5; W, *Granulatisporites adnatoides*, slider No.: ZK4703_ZK10; X, *Calamospora laevigatus*, slider No.: ZK4703_ZK2; Y, *Crassispora orientalis*, slider No.: ZK4703_ZK14; Z, *Calamospora* sp., slider No.: ZK4703_ZK10; AA, *Neoraistrickia rigida*, slider No.: ZK4703_ZK16; BB, *Waltzispora strictura*, slider No.: ZK4703_ZK16; CC–DD, *Triquitrites proratus*, slider No. of cc: ZK4703_ZK16, slider No. of dd: ZK4703_ZK7. Fm., formations; Ass., palynological assemblages 1–5 are indicated.

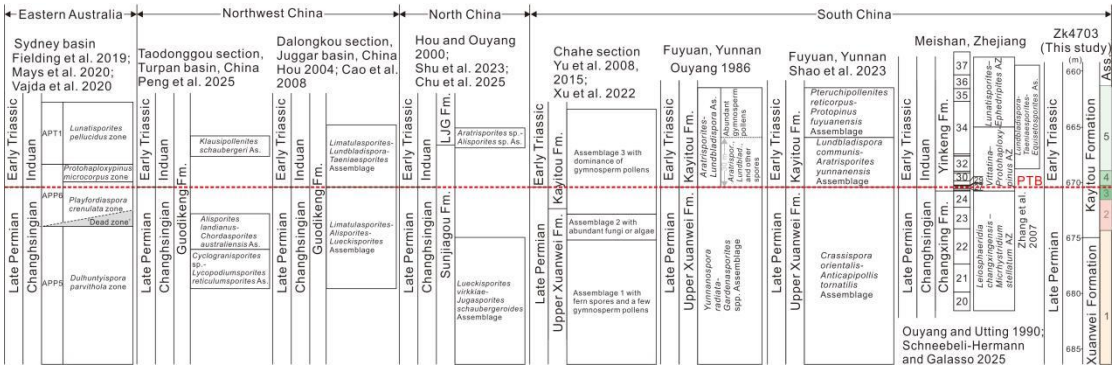


**Figure 5.** The latest Permian to Ealry Triassic palynostratigraphical correlations among ZK4703, previous studies in South China (including Meishan) (Ouyang 1986; Ouyang and Utting 1990; Zhang et al. 2007; Yu et al. 2008, 2015; Xu et al. 2022;

479 Shao et al. 2023; Schneebeli-Hermann and Galasso 2025), North China (Hou and

480 Ouyang 2000; Shu et al. 2023; Chu et al. 2025), northwestern China (Turpan and

481 Juggar basins) (Hou 2004; Cao et al. 2008; Peng et al. 2025) and Eastern Australia

482 (Fielding et al. 2019; Mays et al. 2020; Vajda et al. 2020).

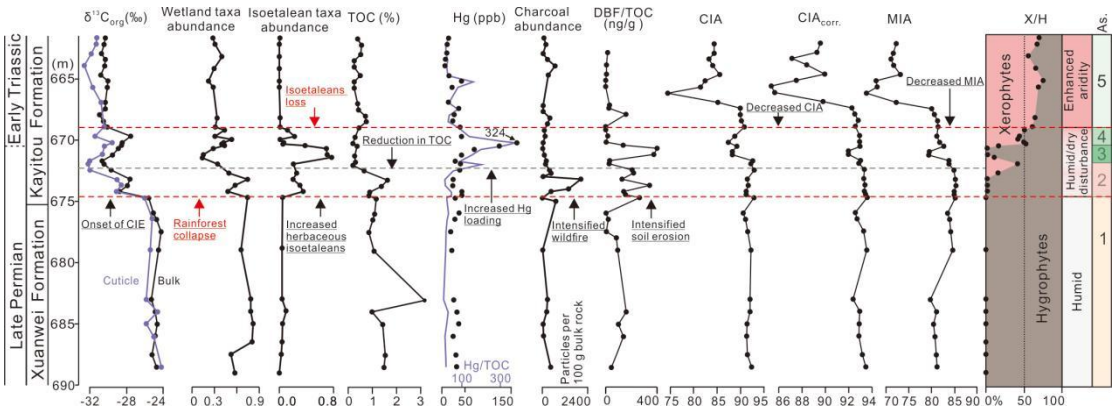


483 **Figure 6.** Sporomorph and chemical weathering intensity data across the Permian–

484 Triassic boundary at ZK4703. Organic carbon isotopes, TOC content, Hg

485 concentration, Hg/TOC ratios and charcoal abundance data are from Chu et al. (2021).

486 DBF/TOC data are from Wu et al. (2023).

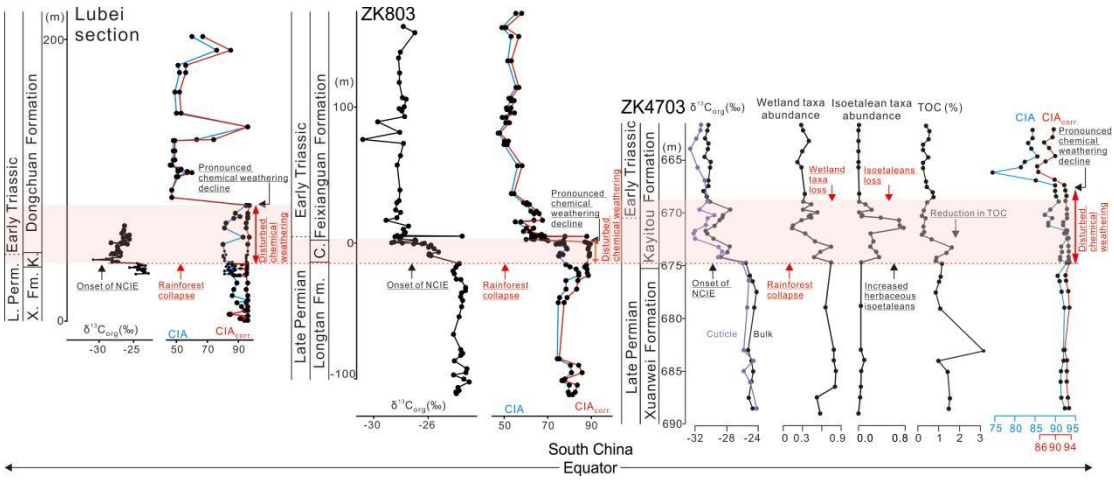


487 **Figure 7.** Disturbance in chemical weathering following rainforest collapse and the
488 subsequent pronounced decline in chemical weathering associated with the loss of
489 wetland flora in southwestern China. Data provenance: For the ZK803 section,
490 Organic carbon isotope ($\delta^{13}C_{org}$) and CIA/CIAcorr records are adapted from Xu et al.
491 (2023). For the Lubei section, data are modified from Zhang et al. (2016, 2021) and
492 Xu et al. (2017). For the ZK4703 section, $\delta^{13}C_{org}$ and TOC data are sourced from Chu
493 et al. (2020, 2021). L. Perm., Late Permian; X. Fm., Xuanwei Formation; K., Kayitou
494 Formation; Fm., Formation; C., Changxing Formation.

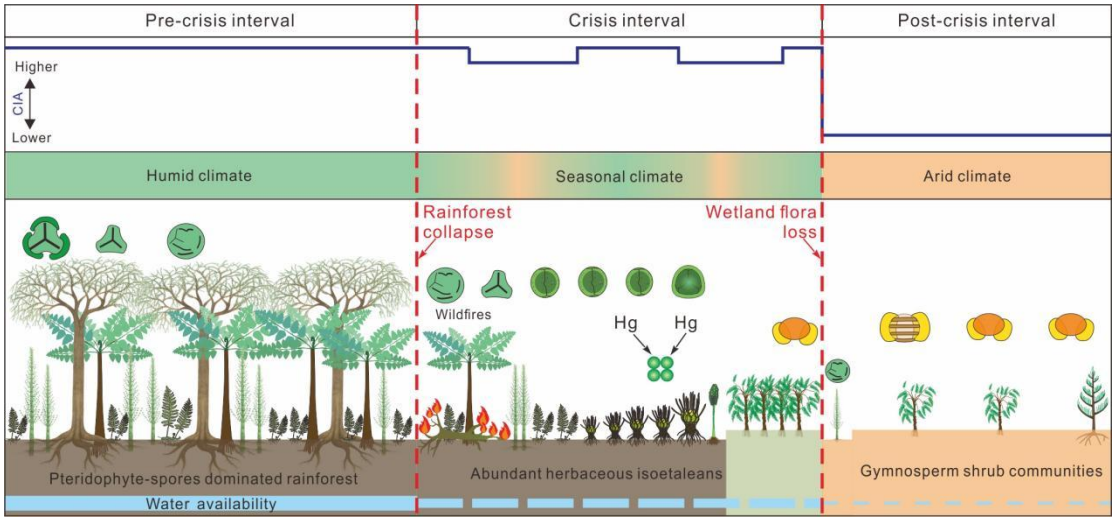


495 **Figure 8.** Reconstruction of terrestrial ecological successions during the Permian–
496 Triassic transition in southwestern China.

497 **Reference**

498 Babechuk, M.G., Widdowson, M., Kamber, B.S., 2014. Quantifying chemical
499 weathering intensity and trace element release from two contrasting basalt
500 profiles, Deccan Trap, India. Chemical Geology, 363, 56–75.
501 Balme, B.E., 1963. Plant microfossils from the Lower Triassic of Western Australia.
502 Palaeontology, 6 (1), 12–40.
503 Benton, M.J., 2016. The Triassic. Current Biology, 26 (23), R1214–R1218.
504 Benton, M.J., 2018. Hyperthermal-driven mass extinctions: killing models during the
505 Permian–Triassic mass extinction. Philosophical Transactions of the Royal
506 Society A: Mathematical, Physical and Engineering Sciences, 376 (2130),
507 20170076.
508 Bercovici, A., Cui, Y., Forel, M.B., Yu, J., Vajda, V., 2015. Terrestrial

509 paleoenvironment characterization across the Permian–Triassic boundary in
510 South China. Journal of Asian Earth Sciences, 98, 225–246.
511 Berner, R.A., 1992. Weathering, plants, and the long-term carbon cycle. Geochimica
512 et Cosmochimica Acta, 56 (8), 3225–3231.
513 Brantley, S.L., Shaughnessy, A., Lebedeva, M.I., Balashov, V.N., 2023. How
514 temperature-dependent silicate weathering acts as Earth's geological thermostat.
515 Science, 379, 382–389.
516 Broutin, J., Yu, J., Shi, X., Shu, W., Xue, Q., 2020. Terrestrial palaeofloral succession
517 across the Permian–Triassic Boundary in the North and South China blocks: a
518 brief review. PalZ, 94, 633–644.
519 Cao, C.Q., Wang, W., Liu, L.J., Shen, S.Z., Summons, R.E., 2008. Two episodes of
520 $^{13}$C-depletion in organic carbon in the latest Permian: evidence from the
521 terrestrial sequences in northern Xinjiang, China. Earth and Planetary Science
522 Letters, 270, 251–257.
523 Cao, Y., Song, H., Algeo, T.J., Chu, D., Du, Y., Tian, L., Wang, Y., Tong, J., 2019.
524 Intensified chemical weathering during the Permian–Triassic transition recorded
525 in terrestrial and marine successions. Palaeogeography, Palaeoclimatology,
526 Palaeoecology, 519, 166–177.
527 Cascales–Miñana, B., Diez, J.B., Gerrienne, P., Cleal, C.J., 2016. A palaeobotanical
528 perspective on the great end-Permian biotic crisis. Historical Biology, 28 (8),
529 1066–1074.
530 Chakravarty, S., Ghosh, S.K., Suresh, C.P., Dey, A.N., Shukla, G., 2012. Deforestation:

causes, effects and control strategies. Global perspectives on sustainable forest management, 1, 1–26.

Chen, J., Guo, Y., Wei, H.B., Liu, H.Y., Ma, R.Y., Xiao, Z., Feng, Z., 2022. Evaluation of chemical weathering proxies by comparing drilled cores versus outcrops and weathering history during the Permian–Triassic transition. Global and Planetary Change, 214, 103855.

Chen, J., Lu, B., Du, L., Lin, M., Shen, S. Z., Montañez, I. P., Feng, Z., 2025. Regional postdeforestation weathering feedback drove diachronous C–S cycle perturbations during the end-Permian crisis. Proceedings of the National Academy of Sciences, 122 (44), e2504841122.

Chu, D., Yu, J., Tong, J., Benton, M.J., Song, H., Huang, Y., Song, T., Tian, L., 2016. Biostratigraphic correlation and mass extinction during the Permian–Triassic transition in terrestrial-marine siliciclastic settings of South China. Global and Planetary Change, 146, 67–88.

Chu, D., Grasby, S.E., Song, H., Corso, J.D., Wang, Y., Mather, T.A., Wu, Y., Song, H., Shu, W., Tong, J., Wignall, P.B., 2020. Ecological disturbance in tropical peatlands prior to marine Permian–Triassic mass extinction. Geology, 48 (3), 288–292.

Chu, D., Dal Corso, J., Shu, W., Haijun, S., Paul, B., Grasby, S.E., van de Schootbrugge, B., Zong, K., Wu, Y., Tong, J., 2021. Metal-induced stress in survivor plants following the end-Permian collapse of land ecosystems. Geology, 49 (6), 657–661.

553 Chu, D., Song, H., Dal Corso, J., Winguth, A.M.E., Gautam, M. D., Wignall, P. B.,
554 Grasby, S.E., Shu, W., Song, H., Song, H., Tian, L., Wu, Y., Tong, J., 2025.
555 Diachronous end-Permian terrestrial crises in North and South China. Geology,
556 53 (1), 55–60.
557 Cox, R., Lowe, D.R., Cullers, R.L., 1995. The influence of sediment recycling and
558 basement composition on evolution of mudrock chemistry in the southwestern
559 United States. Geochimica et Cosmochimica Acta., 59, 2919–2940.
560 Dal Corso, J., Newton, R.J., Zerkle, A.L., Chu, D., Song, H., Song, H., Tian, L., Tong,
561 J., Rocco, T.D., Claire, M.W., Mather, T.A., He, T., Gallagher, T., Shu, W., Wu,
562 Y., Bottrell, S.H., Metcalfe, I., Cope, H.A., Novak, M., Jamieson, R.A., Wignall,
563 P.B., 2024. Repeated pulses of volcanism drove the end-Permian terrestrial crisis
564 in northwest China. Nature Communications, 15, 7628.
565 Diez, J.B., Arche, A., Broutin, J., Bourquin, S., De la Horra, R., Ferrer, J., García-Gil,
566 S., López-Gómez, J., 2014. Palynostratigraphic Data for the Buntsandstein and
567 Muschelkalk Facies from the Iberian Ranges (Spain). In STRATI 2013: First
568 International Congress on Stratigraphy at the Cutting Edge of Stratigraphy.
569 Springer International Publishing, 1067–1071.
570 DiMichele, W.A., Tabor, N.J., Chaney, D.S., and Nelson, W.J., 2006, From wetlands
571 to wet spots: Environmental tracking and the fate of Carboniferous elements in
572 Early Permian tropical floras, in Greb, S.F., and DiMichele, W.A., Wetlands
573 through time: Geological Society of America Special Paper, 399, 223–248.
574 DiMichele, W.A., 2014. Wetland-dryland vegetational dynamics in the Pennsylvanian

575 Ice Age tropics. International Journal of Plant Sciences, 175 (2), 123–164.
576 Dunhill, A.M., Zarzyczny, K., Shaw, J.O., Atkinson, J.W., Little, C.T.S., Beckerman,
577 A.P., 2024. Extinction cascades, community collapse, and recovery across a
578 Mesozoic hyperthermal event. Nature Communications, 15 (1), 1–11.
579 Fan, J.X., Shen, S.Z., Erwin, D.H., Sadler, P.M., MacLeod, N., Cheng, Q.M., Hou,
580 X.D., Yang, J., Wang, X.D., Wang, Y., Zhang, H., Chen, X., Li, G.X., Zhang,
581 Y.C., Shi, Y.K., Yuan, D.X., Chen, Q., Zhang, L.N., Li, C., Zhao, Y.Y., 2020. A
582 high-resolution summary of Cambrian to Early Triassic marine invertebrate
583 biodiversity. Science, 367 (6475), 272–277.
584 Feng, Z., Wei, H.B., Guo, Y., Bomfleur, B., 2018. A conifer-dominated Early Triassic
585 flora from Southwest China. Science Bulletin, 63 (22), 1462–1463.
586 Feng, Z., Wei, H.B., Guo, Y., He, X.Y., Sui, Q., Zhou, Y., Liu, H.Y., Gou, X.D., Lv, Y.,
587 2020a. From rainforest to herbland: New insights into land plant responses to the
588 end-Permian mass extinction, Earth-Science Reviews, 204, 103153.
589 Feng, Z., Wei, H.B., Ye, R.H., Sui, Q., Gou, X.D., Guo, Y., Liu, L.J., Yang, S.L.,
590 2020b. Latest Permian Peltasperm plant from southwest China and its
591 paleoenvironmental implications. Frontiers in Earth Science, 8, 559430.
592 Fielding, C.R., Frank, T.D., McLoughlin, S., Vajda, V., Mays, C., Tevyaw, A.P.,
593 Winguth, A., Winguth, C., Nicoll, R.S., Bocking, M., Crowley, J.L., 2019. Age
594 and pattern of the southern high-latitude continental end–Permian extinction
595 constrained by multiproxy analysis. Nature communications, 10 (1), 1–12.
596 Flores, B.M., Montoya, E., Sakschewski, B., Nascimento, N., Staal, A., Betts, R.A.,

Levis, C., Lapola, D.M., Esquível–Muelbert, A., Jakovac, C., Nobre, C.A., 2024. Critical transitions in the Amazon forest system. Nature, 626 (7999), 555–564.

Frank, T.D., Fielding, C.R., Winguth, A.M.E., Savatic, K., Tevyaw, A., Winguth, C., McLoughlin, S., Vajda, V., Mays, C., Nicoll, R., Bocking, M., 2021. Pace, magnitude, and nature of terrestrial climate change through the end-Permian extinction in southeastern Gondwana. Geology, 49 (9), 1089–1095.

Galfetti, T., Hochuli, P.A., Brayard, A., Bucher, H., Weissert , H., Vigran, J.O., 2007. The Smithian/Spathian boundary event: Evidence for global climatic change in the wake of the end-Permian biotic crisis. Geology, 35 (4), 291–294.

Garzanti, E., Ando, S., France-Lenord, C., Vezzoli, G., Censi, P., Galy, V., Najman, Y., 2010. Mineralogical and chemical variability of fluvial sediments. 1. Bedload sand (Ganga-Brahmaputra, Bangladesh). Earth and Planetary Science Letters, 299, 368–381.

Garzanti, E., Ando, S., France-Lenord, C., Censi, P., Vignola, P., Galy, V., Lupker, M., 2011. Mineralogical and chemical variability of fluvial sediments 2. Suspended-load silt (Ganga-Brahmaputra, Bangladesh). Earth and Planetary Science Letters, 302, 107–120.

Garzanti, E., Resentini, A., 2016. Provenance control on chemical indices of weathering (Taiwan river sands). Sedimentary Geology, 336, 81–95.

Gutiérrez, P.R., Zavattieri, A.M., Ezpeleta, M., 2017. Palynology of the La Veteada Formation (Lopingian) at its type locality, Famatina Range, La Rioja Province, Argentina. Spores. Ameghiniana, 54, 441–464.

619 Hammer, Ø., Harper, D.A.T., 2001. Past: paleontological statistics software package
620 for educaton and data anlysis. Palaeontologia electronica, 4(1): 1–31.
621 Hankel, O., 1992. Late Permian to early triassic microfloral assemblages from the
622 Maji ya chumvi formation, Kenya. Review of Palaeobotany and Palynology, 72
623 (1–2), 129–147.
624 Hochuli, P.A., Vigran, J.O., Hermann, E., Bucher, H., 2010a. Multiple climatic
625 changes around the Permian–Triassic boundary event revealed by an expanded
626 palynological record from mid-Norway. GSA Bulletin, 122 (5–6), 884–896.
627 Hochuli, P.A., Hermann, E., Vigran, J.O., Bucher, H., Weissert, H., 2010b. Rapid
628 demise and recovery of plant ecosystems across the end-Permian extinction
629 event. Global and Planetary Change, 74, 144–155.
630 Hou, J., Ouyang, S., 2000. Palynoflora from the Sunjiagou Formation in Liulin county,
631 Shanxi province. Acta Palaeontologica Sinica, 39 (3): 356–368.
632 Hou, J., 2004. Two sporo-pollen assemblages of Guodikeng formation and discussion
633 on the Permo-Triassic boundary in Junggar Basin, Xinjiang. In: Editorial
634 Committee of Professional Papers of Stratigraphy and Palaeontology of Chinese
635 Academy of Geological Sciences (Ed.), Professional papers of Stratigraphy and
636 Palaeontology, 28. Geological Publishing House, Beijing, 177–204.
637 Hull, P.M., Darroch, S.A.F., 2017. Mass extinctions and the structure and function of
638 ecosystems. The Paleontological Society Papers, 19, 115–156.
639 Jewuła, K., Trela, W., Fijałkowska-Mader, A., 2021. Sedimentary and pedogenic
640 record of seasonal humidity during the Permian–Triassic transition on the SE

margin of Central European Basin (Holy Cross Mountains, Poland). Palaeogeography, Palaeoclimatology, Palaeoecology, 564, 110154.

Juggins, S., 2007. C2 Version 1.5 User guide. Software for ecological and palaeoecological data analysis and visualisation. Newcastle University, Newcastle upon Tyne, UK. 73pp.

Kump, L.R., Brantley, S.L., Arthur, M.A., 2000. Chemical weathering, atmospheric $CO_2$ and climate. Annual Review of Earth and Planetary Science, 28, 611–667.

Lancaster, L.T., Humphreys, A.M., 2020. Global variation in the thermal tolerances of plants, Proceedings of the National Academy of Sciences, 117 (24) 13580–13587.

Larsen, I.J., Eger, A., Almond, P.C., Thaler, E.A., Rhodes, J.M., Prasicek, G., 2023. The influence of erosion and vegetation on soil production and chemical weathering rates in the Southern Alps, New Zealand. Earth and Planetary Science Letters, 608, e118036.

Lindström, S., McLoughlin, S., 2007. Synchronous palynofloristic extinction and recovery after the end-Permian event in the Prince Charles Mountains, Antarctica: Implications for palynofloristic turnover across Gondwana. Review of Palaeobotany and Palynology, 145, 89–122.

Liu, F., Peng, H., Bomfleur, B., Kerp, H., Zhu, H., Shen, S., 2020. Palynology and vegetation dynamics across the Permian–Triassic boundary in southern Tibet. Earth-Science Reviews, 209, 103278.

Looy, C.V., Collinson, M.E., Cittert, J.H.V.K.V., Visscher, H., Brain, A.P., 2005. The ultrastructure and botanical affinity of end–Permian spore tetrads. International

663 Journal of Plant Sciences, 166 (5), 875–887.
664 Looy, C.V., van Konijnenburg–van Cittert, J.H., Duijnstee, I.A., 2021. Proliferation of
665 isoëtalean lycophytes during the Permo–Triassic biotic crises: a proxy for the
666 state of the terrestrial biosphere. Frontiers in Earth Science, 9, p.55.
667 Mays, C., Vajda, V., Frank, T.D., Fielding, C.R., Nicoll, R.S., Tevyaw, A.P.,
668 McLoughlin, S., 2020. Refined Permian–Triassic floristic timeline reveals early
669 collapse and delayed recovery of south polar terrestrial ecosystems. GSA
670 Bulletin, 132 (7–8), 1489–1513.
671 Mays, C., McLoughlin, S., Frank, T.D., Fielding, C.R., Slater, S.M., Vajda, V., 2021.
672 Lethal microbial blooms delayed freshwater ecosystem recovery following the
673 end-Permian extinction. Nature Communications, 12, 5511.
674 McElwain, J.C., Punyasena, S.W., 2007. Mass extinction events and the plant fossil
675 record. Trends in ecology & evolution, 22 (10), 548–557.
676 McLennan, S.M., 1993. Weathering and global denudation. The Journal of Geology,
677 101(2), 295–303.
678 McLoughlin, S., Nicoll, R.S., Crowley, J.L., Vajda, V., Mays, C., Fielding, C.R.,
679 Frank, T.D., Wheeler, A., Bocking, M., 2021. Age and Paleoenvironmental
680 Significance of the Frazer Beach Member—A New Lithostratigraphic Unit
681 Overlying the End-Permian Extinction Horizon in the Sydney Basin, Australia.
682 Frontiers in Earth Science, 8, e600976.
683 Nesbitt, H.W., Young, G.M., 1982. Early Proterozoic climates and plate motion
684 inferred from major element chemistry of lutites. Nature 299, 715–717.

685 Nowak, H., Schneebeli–Hermann, E., Kustatscher, E., 2019. No mass extinction for
686 land plants at the Permian–Triassic transition. Nature Communications, 10 (1),
687 384.
688 Ouyang, S., 1986. Palynology of Upper Permian and Lower Triassic strata of Fuyuan
689 district, Eastern Yunnan. Science Press, 1–122.
690 Ouyang, S., Utting, J., 1990. Palynology of upper Permian and lower triassic rocks,
691 Meishan, Changxing County, Zhejiang province, China. Review of Palaeobotany
692 and Palynology, 66 (1–2), 65–103.
693 Panahi, A., Young, G.M., Rainbird, R.H., 2000. Behavior of major and trace elements
694 (including REE) during Paleoproterozoic pedogenesis and diagenetic alteration
695 of an Archean granite near Ville Marie, Québec, Canada. Geochim. Cosmochim.
696 Acta, 64, 2199–2220.
697 Peng, H., Yang, W., Wan, M., Liu, J., Liu, F., 2025. Refugium amidst ruins:
698 Unearthing the lost flora that escaped the end-Permian mass extinction. Science
699 Advance, 11, 5614.
700 Retallack, G.J., Veevers, J.J., Morante, R., 1996. Global coal gap between Permian–
701 Triassic extinction and Middle Triassic recovery of peat-forming plants. GSA
702 Bulletin, 108 (2), 195–207.
703 Schneebeli–Hermann, E., Kürschner, W.M., Kerp, H., Bomfleur, B., Hochuli, P.A.,
704 Bucher, H., Ware, D., Roohi, G., 2015. Vegetation history across the Permian–
705 Triassic boundary in Pakistan (Amb section, Salt Range). Gondwana Research,
706 27, 911–924.

Schneebeli–Hermann, E., Hochuli, P. A., Bucher, H., 2017. Palynofloral associations before and after the Permian–Triassic mass extinction, Kap Stosch, East Greenland. Global and Planetary Change, 155, 178–195.

Schneebeli-Hermann, E., 2020. Regime shifts in an Early Triassic subtropical ecosystem. Frontiers in Earth Science, 8, e588696.

Schneebeli-Hermann, E., Galasso, F., 2025. Resilient gymnosperms: reassessing floral dynamics at the Permian–Triassic extinction in Meishan. Review of Palaeobotany and Palynology, 341, e105373.

Scotese, C.R., 2021. An atlas of phanerozoic paleogeographic maps: the seas come in and the seas go out. Annual Review of Earth and Planetary Sciences, 49, 679–728.

Sephton, M.A., Jiao, D., Engel, M.H., Looy, C.V., Visscher, H., 2015. Terrestrial acidification during the end-Permian biosphere crisis? Geology, 43 (2), 159–162.

Shao, L., Hua, F., Wang, J., Ji, X., Yan, Z., Zhang, T., Wang, X., Ma, S., Jones, T., Lu, H., 2023. Palynological dynamics in the late Permian and the Permian–Triassic transition in southwestern China. Palaeogeography, Palaeoclimatology, Palaeoecology, 619, 111540.

Shu, W., Tong, J., Yu, J., Hilton, J., Benton, M.J., Shi, X., Diez, J.B., Wignall, P.B., Chu, D., Tian, L., Yi, Z., Mao, Y., 2022. Permian−Middle Triassic floral succession in North China and implications for the great transition of continental ecosystems. Geological Society of America Bulletin, 135(7–8): 1747–1767.

Smith, A.H.V., Butterworth, M.A., 1967. Miospores in the coal seams of the

729 Carboniferous of Great Britain. Special Papers in Palaeontology, 1, 1–324.
730 Stanley, S.M., 2016. Estimates of the magnitudes of major marine mass extinctions in
731 earth history. Proceedings of the National Academy of Sciences, 113 (42),
732 e6325–e6334.
733 Sun, Y., Farnsworth, A., Joachimski, M.M., Wignall, P.B., Krystyn, L., Bond, D.P.G.,
734 Ravidà, D.C.G., Valdes, P. J., 2024. Mega El Niño instigated the end-Permian
735 mass extinction. Science, 385, 1189–1195.
736 Tilman, D., Isbell, F., Cowles, J.M., 2014. Biodiversity and ecosystem functioning.
737 Annual Review of Ecology, Evolution, and Systematics, 45, 471–493.
738 Vajda, V., McLoughlin, S., Mays, C., Frank, T.D., Fielding, C.R., Tevyaw, A., Lehsten,
739 V., Bocking, M., Nicoll, R.S., 2020. End-Permian (252 Mya) deforestation,
740 wildfires and flooding—an ancient biotic crisis with lessons for the present.
741 Earth and Planetary Science Letters, 529, 115875.
742 Vajda, V., Grice, K., Krüger, A., Lee, S., Shi, G.R., 2023. End-Permian marine
743 ecosystem collapse was a direct consequence of deforestation: Evidence from the
744 Kockatea Shale of the Perth Basin, Western Australia. Evolving Earth, 1, 100027.
745 Visscher, H., van der Zwan, W.A., 1981, Palynology of the circum-Mediterranean
746 Triassic: Phytogeographical and palaeoclimatological implications: Geologische
747 Rundschau, 70, 625–636.
748 Visscher, H., Looy, C.V., Collinson, M.E., Brinkhuis, H., van Konijnenburg-van
749 Cittert, J.A.H., Kürschner, W.M., Sephton, M.A., 2004. Environmental
750 mutagenesis during the end-Permian ecological crisis. Proceedings of the

National Academy of Sciences of the United States of America, 101 (35), 12952–12956

Visscher, H., Sephton, M.A., Looy, C.V., 2011. Fungal virulence at the time of the end-Permian biosphere crisis? Geology, 39 (9), 883–886.

Wignall, P.B., Chu, D., Hilton, J.M., Dal Corso, J., Wu, Y., Wang, Y., Atkinson, J., Tong, J., 2020. Death in the shallows: The record of Permo-Triassic mass extinction in paralic settings, southwest China, Global and Planetary Change, 189, 103176.

Wu, J., Chu, D., Luo, G., Wignall, P.B., Algeo, T.J., Xie, S., 2023. Stepwise deforestation during the Permian-Triassic boundary crisis linked to rising temperatures. Earth and Planetary Science Letters, 620, e118350.

Wu, Y., Chu, D., Tong, J., Song, H., Dal Corso, J., Wignall, P.B., Song, H., Du, Y., Cui, Y., 2021. Six-fold increase of atmospheric $pCO_2$ during the Permian–Triassic mass extinction. Nature communications, 12 (1), 1–8.

Xu, G., Feng, Q., Deconinck, J.F., Shen, J., Zhao, T., Young, A.L., 2017. High-resolution clay mineral and major elemental characterization of a Permian–Triassic terrestrial succession in southwestern China: Diagenetic and paleoclimatic/paleoenvironmental significance. Palaeogeography, Palaeoclimatology, Palaeoecology, 481: 77–93.

Xu, G., Shen, J., Algeo, T.J., Yu, J., Feng, Q., Frank, T.D., Fielding, C.R., Yan, J., Deconinck, J.F., Lei, Y., 2023. Limited change in silicate chemical weathering intensity during the Permian–Triassic transition indicates ineffective climate

773 regulation by weathering feedbacks. Earth and Planetary Science Letters, 616,
774 118235.
775 Xu, Z., Hilton, J., Yu, J., Wignall, P.B., Yin, H., Xue, Q., Ran, W., Li, H., Shen, J.,
776 Meng, F., 2022. End Permian to Middle Triassic plant species richness and
777 abundance patterns in South China: coevolution of plants and the environment
778 through the Permian–Triassic transition. Earth-Science Reviews, 232, 104136.
779 Xu, Z., Yu, J., Yin, H., Merdith, A.S., Hilton, J., Allen, B.J., Gurung, K., Wignall, P.B.,
780 Dunhill, A.M., Shen, J., Schwartzman, D., Goddéris, Y., Donnadieu, Y., Wang, Y.,
781 Zhang, Y., Poulton, S.W., Mills, B.J.W., 2025. Early Triassic super-greenhouse
782 climate driven by vegetation collapse. Nature Communications, 16, e5400.
783 Yang, J., Cawood, P. A., Condon, D. J., Liu, J., Deng, X., Wang, J., Du, Y., Yuan, D.,
784 2022. Anomalous weathering trends indicate accelerated erosion of tropical
785 basaltic landscapes during the Permo-Triassic warming. Earth and Planetary
786 Science Letters, 577, 117256.
787 Yu, J., Li, H., Zhang, S., Yang, F., Feng, Q., 2008. Timing of the terrestrial Permian–
788 Triassic boundary biotic crisis: Implications from U-Pb dating of authigenic
789 zircons. Science in China Series D: Earth Sciences, 51(11), 1633–1645.
790 Yu, J., Broutin, J., Huang, Q., Grauvogel–Stamm, L., 2010. *Annalepis*, a pioneering
791 lycopsid genus in the recovery of the Triassic land flora in South China. Comptes
792 Rendus Palevol, 9 (8), 479–486.
793 Yu, J., Broutin, J., Chen, Z., Shi, X., Li, H., Chu, D., Huang, Q., 2015. Vegetation
794 changeover across the Permian–Triassic Boundary in Southwest China:

795 Extinction, survival, recovery and palaeoclimate: A critical review. Earth-Science
796 Reviews, 149, 203–224.
797 Zhang, H., Cao, C.Q., Liu, X.L., Mu, L., Zheng, Q.F., Liu, F., Xiang, L., Liu, L.J.,
798 Shen, S.Z., 2016. The terrestrial end-Permian mass extinction in South China.
799 Palaeogeography, Palaeoclimatology, Palaeoecology, 448, 108–124.
800 Zhang, H., Zhang, F., Chen, J., Erwin, D.H., Syverson, D.D., Ni, P., Rampino, M., Chi,
801 Z., Cai, Y., Xiang, L., Li, W., Liu, S., Wang, R., Wang, X., Feng, Z., Li, H.,
802 Zhang, T., Cai, H., Zheng, W., Cui, Y., Zhu, X., Hou, Z., Wu, F., Xu, Y.,
803 Planavsky, N., Shen, S., 2021. Felsic volcanism as a factor driving the end-
804 Permian mass extinction. Science Advances, 7 (47), e1390.
805 Zhang, K., Tong, J., Shi, G.R., Lai, X., Yu, J., He, W., Peng, Y., Jin, Y., 2007. Early
806 Triassic conodont–palynological biostratigraphy of the Meishan D Section in
807 Changxing, Zhejiang Province, South China. Palaeogeography,
808 Palaeoclimatology, Palaeoecology, 252: 4–23.
809 Zheng, R.H., 2011. China Pre-Mesozoic Structural Sequence and Lithofacies
810 Paleogeography Atlas. Geological Publishing House, Beijing (In Chinese).